Anisotropy of the penetration depth in superconducting tin*

P. C. L. Tai,† M. R. Beasley,‡ and M. Tinkham
Physics Department and Division of Engineering and Applied Physics, Harvard University, Cambridge, Massachusetts 02138
(Received 19 June 1974)

The temperature dependence and anisotropy of the penetration depth $\lambda(T)$ in superconducting tin was measured using a superconducting magnetometer. Single bulk crystals of tin were used as samples to measure the anisotopy with respect to crystallographic orientations. Considerable anisotropy was found with respect to $\hat{j}$, the shielding-current direction, and $\hat{n}$, the direction of the normal to the sample plane surfaces. These data are compared to a simple theory of nonlocal anisotropy. They are also fitted to the BCS theory by varying parameters.

I. INTRODUCTION

Research on the magnetic field penetration into superconductors and the associated penetration depth λ played an important role in the development of our understanding of superconductivity. However, despite its long history, the theory of the phenomenon is not complete and the experimental measurements are not definitive. This is especially so with respect to the anisotropy of λ, where the complex anisotropies of the Fermi surface and of the energy gap have to be considered. The previous measurements of[1-5] λ were deficient in that: (i) ac measurements were made so that corrections to zero frequency were sometimes necessary; (ii) cylindrical samples were used. The second deficiency is significant in measuring the anisotropy in single crystals because nonlocal anisotropy, which can arise even in cubic superconductors, is strongest when the superconductor has a plane-surface boundary. The curved surface of a cylindrical superconductor will partially average out the nonlocal anisotropic effect. The present experiment avoids the above-mentioned drawbacks. We used a dc SQUID (superconducting quantum interference device) magnetometer to measure the static penetration depth directly, and we used disk-shaped single crystals of tin with polished flat surfaces as samples. Anisotropy in λ is found with respect to $\hat{j}$, the shielding-current direction, and $\hat{n}$, the normal to the flat sample surfaces. As reported earlier by Tai, Beasley, and Tinkham,[6] the anisotropy with respect to $\hat{n}$ is a demonstration of the nonlocal anisotropy due to the nonlocal electrodynamic relation between $\vec{j}$ and $\vec{A}$ in the superconductor.

II. THEORY

The static penetration depth is defined in the semi-infinite plane geometry (the superconductor occupying the half-space $z \geq 0$) as

$$\lambda = \frac{1}{B(0)} \int_0^\infty dz\, B(z) , \tag{1}$$

where $B(z)$ is the magnetic-flux density penetrating at a depth z below the plane surface. The external field at $z < 0$ is $B(0)$ and is parallel to the x-y plane. The present experiment directly measures the changes in the total penetrated flux with changing temperature. The magnitude of this penetration depth depends on the electromagnetic response of the superconductor.

London[7] assumed this response to be a local one:

$$\vec{j}(\vec{r}) = -(1/c\Lambda)\, \vec{A}(\vec{r}) , \tag{2}$$

where $\vec{j}$ is the shielding-current density induced by the vector potential $\vec{A}$, and Λ is a constant of the superconductor. Combining this theory with the two-fluid thermodynamic model of Gorter and Casimir[8] gave a temperature dependence of λ:

$$\lambda(t) = (c^2\Lambda/4\pi)^{1/2}\, (1-t^4)^{-1/2} = \lambda(0)\, Y(t) , \tag{3}$$

where $t = T/T_c$, and $Y(t)$ is defined to be $(1-t^4)^{-1/2}$.

Pippard[1] modified London's equation into a nonlocal one:

$$\vec{j}(\vec{r}) = \frac{-3}{4\pi c \xi_0 \Lambda(T)} \int d\vec{r}'\, \frac{\vec{R}[\vec{R}\cdot\vec{A}(\vec{r}')]}{R^4}\, e^{-R/\xi_0} , \tag{4}$$

where ξ_0 is the coherence length for the pure metal and $\vec{R} = \vec{r} - \vec{r}'$. Here Pippard made the assumption that $\vec{j}(\vec{r})$ is not uniquely determined by the vector potential $\vec{A}(\vec{r})$ just at the point $\vec{r}$, but is proportional to an average of $\vec{A}$ in the neighborhood of $\vec{r}$, taken over a volume of characteristic size ξ_0 as specified by (4). This nonlocal modification is supported by the microscopic theory of BCS,[9] which results in a similar nonlocal equation (in the clean limit):

$$\vec{j}(\vec{r}) = \frac{-3}{4\pi c \xi_0 \Lambda(T)} \int d\vec{r}'\, \frac{\vec{R}[\vec{R}\cdot\vec{A}(\vec{r}')]}{R^4}\, J(R,T) . \tag{5}$$

The function $J(R, T)$ is not very temperature dependent and describes the spatial range of the nonlocality. It is similar in form to the exponential factor in Pippard's Eq. (4). The coherence length ξ_0 is found to be $\hbar v_F/\pi\Delta(0)$, where $\Delta(0)$ is the su-

perconducting energy gap at $T = 0$.

It should be noted that the above theories are derived using isotropic models. In particular, the Pippard equation can be arrived at by analogy with the Chambers relation for the anomalous skin effect in normal metals,[10] which is valid only for a metal with spherical Fermi surface. The anisotropy in the electromagnetic response of the superconductor arises from the anisotropy of the Fermi surface[11] and that of the energy gap.[12] It is difficult to take fully into account these complex anisotropies. Litovchenko[13] considered the simplified problem of an isotropic energy gap but a Fermi surface which is (i) ellipsoidal or (ii) cylindrical. The penetration depth is found to be anisotropic. Nam[14] used a Green's-function formulation to calculate the electromagnetic response kernel. His method is general and is applicable to strong coupling and anisotropic superconductors. However, the problem remains of applying the general results to calculate the complicated anisotropies.

In spite of these difficulties, the form of the anisotropy of λ for the plane-surface geometry used in the present experiments can be deduced from the following simple treatment.[6,15] The Chambers relation can be generalized to nonspherical Fermi surfaces by introducing an anisotropy factor into the integral over $\vec{R}$.[15,16] We proceed to make a similar generalization of the nonlocal equation (5) for the anisotropic superconductor. The factors ξ_0, $\Lambda(T)$, and $J(R, T)$ are anisotropic quantities. The coherence length $\xi_0 = \hbar v_F/\pi\Delta(0)$ depends on the anisotropy of the Fermi velocity and of the energy gap. This means that the function $J(R, T)$ is also anisotropic since its spatial range is ξ_0. The London parameter $\Lambda(0)$ is dependent on the anisotropy of the Fermi surface; and $\Lambda(T)$ is dependent on the anisotropic energy gap $\Delta(T)$ in addition. These anisotropies are with respect to $\hat{v}$, the direction of the electron velocity, and thus to the direction $\hat{R}$ in the integral in (5). Instead of writing out in full the various anisotropies, we include all the anisotropic quantities in an anisotropy factor $F(\hat{R})$ so that we can rewrite (5) as:

$$\vec{j}(\vec{r}) = \frac{-3}{4\pi c \bar{\xi}_0 \bar{\Lambda}(T)} \int d\vec{R} \frac{\vec{R}[\vec{R}\cdot\vec{A}(\vec{r}')]}{R^4} \bar{J}(R, T) F(\hat{R}) , \tag{6}$$

where the upper bars indicate averages over $\hat{R}$. $F(\hat{R})$ will be unity for isotropic superconductors.

In the local limit, where $\lambda \gg \xi_0$, the vector potential $\vec{A}$ can be taken out of the integral and, after some simplification,

$$\vec{j}(\vec{r}) = -\frac{1}{c}\left(\frac{3}{4\pi\bar{\Lambda}(T)} \int d\Omega \hat{R}\hat{R} F(\hat{R})\right) \cdot \vec{A}(\vec{r}) , \tag{7}$$

which is a tensorial local relation as expected.

In the nonlocal limit, where $\lambda \ll \xi_0$, we can make use of Pippard's "ineffectiveness" concept[1,17] to visualize the situation. In this picture, only those electrons moving almost parallel to the superconductor surface will be "effective" in shielding the magnetic field. These effective electrons will occupy regions in the Fermi surface where $\hat{v}$ (the normal to the Fermi surface) will be almost parallel to the superconductor surface (to within an angle $\approx \lambda/\xi_0$). If the superconductor boundary is a plane with normal $\hat{n}$, these effective regions will be uniquely defined. If $\hat{n}$ is changed by changing the orientation of the superconductor surface, different regions on the Fermi surface will become "effective." The anisotropy factor $F(\hat{R})$ in (6) will contribute differently to the integral for different "effective" regions. This argument also applies to the energy-gap anisotropy with respect to $\hat{v}$. Thus, we shall expect the electrodynamic response and hence λ to be dependent on the direction $\hat{n}$. This dependence is in addition to the dependence on $\hat{A}$ or $\hat{j}$ which appears explicitly in (6); we shall refer to it as the nonlocal anisotropy. If the superconductor does not have a plane surface, then $\hat{n}$ is not unique and the nonlocal anisotropy is averaged over the set of $\hat{n}$. In the case of cylindrical samples, $\hat{n}$ rotates around a circle, and the nonlocal anisotropy is very much diminished. Since the present experiment uses superconductors with plane surfaces as samples, the nonlocal anisotropy is not obscured. In addition, the planar sample also has the advantage of approximating the semi-infinite superconductor geometry that is used in many theories; thus comparisons with theories are simplified.

We can proceed with the calculation of the penetration depth in the nonlocal limit using (6) as follows. We set up our coordinate axes with z parallel to $\hat{n}$. For notational simplicity, the direction of x is chosen to be along an axis of symmetry in the plane of the superconductor surface. Then, the component of $\vec{j}$ parallel to $\vec{A}$ is:

$$j_A(z) = \frac{-3}{4\pi c \bar{\xi}_0 \bar{\Lambda}(T)} \int d\vec{R} \frac{(\vec{R}\cdot\hat{A})^2 A(z')}{R^4} \bar{J}(R, T) F(\hat{R}) .$$

In the above, $\vec{j}$ and $\vec{A}$ are functions of z alone, and $z' = z - R_z$. Using polar coordinates (R, θ, φ) for $\vec{R}$, with z as the polar axis, this reduces to:

$$\begin{aligned} j_A(z) = \frac{-3}{4\pi c \bar{\xi}_0 \bar{\Lambda}(T)} & \int_0^\infty d\vec{R} \bar{J}(R, T) \\ & \times \int_0^\pi d\theta \sin^3\theta A(z - R\cos\theta) \\ & \times \int_0^{2\pi} d\varphi \cos^2(\varphi - \varphi_A) F(\theta, \varphi) , \end{aligned} \tag{8}$$

where φ_A is the angle between $\vec{A}$ and the x axis, both of which are in the plane of the surface. In

the nonlocal limit ($\lambda \ll \xi_0$), this integral can be simplified by the use of the "ineffectiveness" concept. Since $\bar{J}(R, T)$ limits the important range of R to $R \lesssim \xi_0$ and A is big only when $R\cos\theta \lesssim \lambda$, the integral will be dominated by the region $\cos\theta \lesssim \lambda/\xi_0$. This, in the limit $\lambda \ll \xi_0$, restricts the significant range of θ to that bounded by $\frac{1}{2}\pi \pm \beta\lambda/\xi_0$, where $\beta \simeq 1$. If we assume that, in this small range of θ, $F(\theta, \varphi)$ is approximately independent of θ, then the kernel in (8) is proportional to a φ_A-dependent multiplicatory factor:

$$\int_0^{2\pi} d\varphi \cos^2(\varphi - \varphi_A) F(\tfrac{1}{2}\pi, \varphi)$$
$$= \pi[\langle F(\tfrac{1}{2}\pi, \varphi)\rangle + \langle F(\tfrac{1}{2}\pi, \varphi)\cos 2\varphi\rangle \cos 2\varphi_A]$$
$$= \pi[\langle F(\hat{n}, \varphi)\rangle + \langle F(\hat{n}, \varphi)\cos 2\varphi\rangle \cos 2\varphi_A], \quad (9)$$

where the angular brackets denote angular averages over φ. We have used the fact that x (where $\varphi = 0$) is directed along one symmetry axis on the x-y plane and thus $\langle F(\frac{1}{2}\pi, \varphi)\sin 2\varphi\rangle = 0$. Also, we have written $\langle F\rangle$ as a function of $\hat{n}$ to indicate that these angular averages are $\hat{n}$ dependent.

This φ_A-dependent multiplicatory factor in the kernel leads to a similar φ_A dependence in the penetration depth. Using an argument similar to Pippard's,[17] we can see that the density of effective electrons is now reduced and anisotropic; its φ_A dependence is given by the factor above:

$$n_s' = n_s \left(\frac{3\beta\lambda}{2\bar{\xi}_0(\hat{n})}\right)[\langle F(\hat{n}, \varphi)\rangle + \langle F(\hat{n}, \varphi)\cos 2\varphi\rangle \cos 2\varphi_A],$$

where n_s is the density of superconducting electrons defined in the London limit by $\lambda_L^2 = mc^2/4\pi n_s e^2$, and $\bar{\xi}_0(\hat{n})$ is the average value of the coherence length in the plane perpendicular to n. Putting this effective density n_s' into the formula $\lambda^2 = mc^2/4\pi n_s' e^2$, we have:

$$\lambda = [(2/3\beta)\lambda_L^2 \xi_0(\hat{n})]^{1/3} \{\langle F(\hat{n}, \varphi)\rangle [1 + \delta(\hat{n})\cos 2\varphi_A]\}^{-1/3}, \quad (10)$$

where

$$\delta(\hat{n}) = \langle F(\hat{n}, \varphi)\cos 2\varphi\rangle / \langle F(\hat{n}, \varphi)\rangle . \quad (11)$$

$\delta(\hat{n})$ is a measure of the anisotropy of λ with respect to φ_A. In the limit of small anisotropy, $\delta(\hat{n}) \ll 1$, the above simplifies to:

$$\lambda = [(2/3\beta)\lambda_L^2 \xi_0(\hat{n})]^{1/3} \langle F(\hat{n}, \varphi)\rangle^{-1/3} \times [1 + \tfrac{1}{3}\delta(\hat{n})(1 - 2\cos^2\varphi_A)] . \quad (12)$$

The average value of λ for a given $\hat{n}$ is given by the product of the first two factors, while the anisotropy with respect to φ_A is given by the final factor. For fixed $\hat{n}$, λ depends on the direction $\hat{A}$ through the factor $\delta(\hat{n})\cos^2\varphi_A$. This linear dependence on $\cos^2\varphi_A$ reflects the behavior of a two-dimensional tensorial relation, just as would be found in the local limit. The results of Litovchenko[13] using an ellipsoidal Fermi surface agree with this conclusion. While the variation with $\cos^2\varphi_A$ is a general property, the particular dependence on microscopic parameters in (12) is, of course, specific to the nonlocal limit.

III. EXPERIMENTAL TECHNIQUE

The present experiment uses a dc SQUID magnetometer to measure the change in the magnetic flux penetrating the superconductor in a uniform dc magnetic field as its temperature is varied. The temperature dependence of the static magnetic field penetration depth is inferred. Since a dc method is used, corrections for high-frequency effects[2] are not necessary. The samples used are oriented single crystals of tin. They are disk shaped with two flat surfaces so that the anisotropy, in particular the nonlocal anisotropy, can be measured. With this method, only changes in the penetration depth with temperature are measured; absolute measurements are not possible. Using a different dc method, however, Anderson and Ginsberg[18] have measured the absolute value of the London penetration depth in thin polycrystalline films.

The magnetometer design is similar to the one used by Gollub *et al.*[19] A schematic diagram of the apparatus is shown in Fig. 1. The SQUID used is a dc double-point-contact one, in which the contacts were made by pressing together two 0.001-in.-thick niobium foils at two spots, enclosing an open area measuring 2 mm×2 mm. This sensing area is magnetically coupled to the sample via a dc superconducting flux transporter. This method isolates the sample from the SQUID and insures that the environment of the SQUID is unaffected by the heating or the rotation of the sample. The sensing coil L_p (transporter primary) is a six-turn coil tightly glued onto a rectangular holder made of red brass. The sample is placed in the transporter primary with its midplane just above the primary coil as indicated in the figure. By this means the sample can be rotated about its axis without disturbing the flux transporter while still maintaining good coupling between the sample and transporter primary. The transporter secondary L_s is placed in the sensing area of the SQUID. A small feedback-coupling coil L_c is inserted in the transporter circuit so that an external feedback current can be inductively coupled so as to null the current I in the transporter. Thermal switches are used to break the superconducting transporter loop when the applied field is changed and to allow trapped flux to escape.

The SQUID is dc current biased near its critical current. A small 300-Hz modulating field is coupled into the SQUID through the coupling coil L_c,

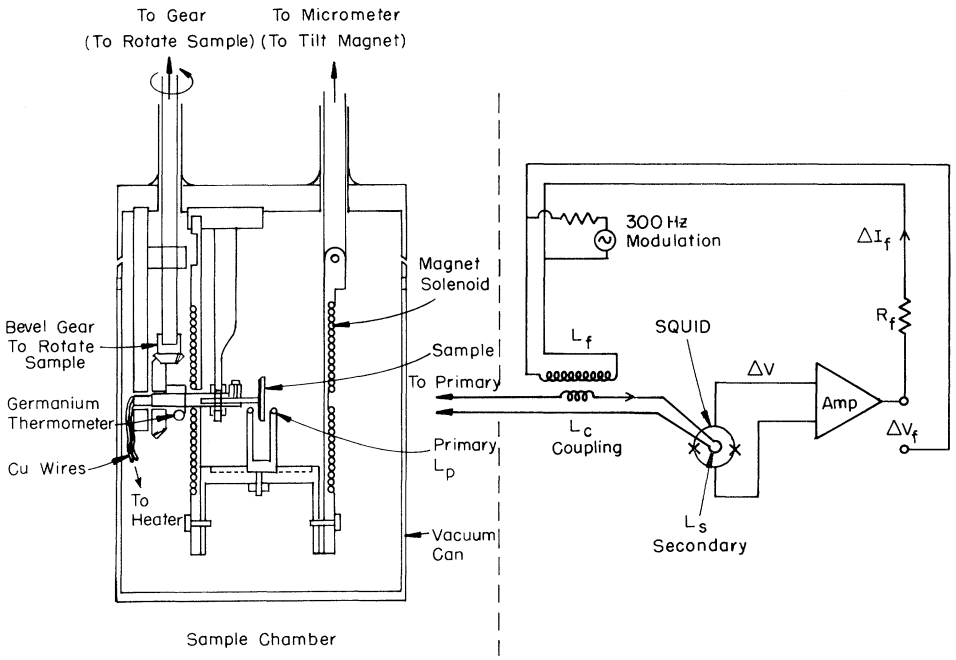

FIG. 1. Schematic diagram of the experimental apparatus. Note that the superconducting flux transporter links the sample with the SQUID.

thus producing a 300-Hz voltage signal across the interferometer. This voltage signal ΔV is sensitive to the magnetic flux transported into the SQUID, and is detected by a lock-in amplifier through a X100 transformer. The dc output of the lock-in amplifier is fed back into the transporter circuit through L_c in a negative feedback manner to keep the transporter current I nulled, as mentioned above. For high loop gain, this feedback current ΔI_f is proportional to the flux change in the sample and is independent of the SQUID characteristics.

The magnetometer is shielded against magnetic noise and stray electrical pick up by the following methods: (i) enclosing the whole experimental apparatus inside an rf-shielded enclosure manufactured by the Ray Proof Corp.; (ii) individually enclosing the SQUID, the flux transporter, and the sample chamber in superconducting lead shields; (iii) using rf filters on feedback and SQUID current leads; and (iv) reducing the ambient earth's magnetic field to less than 1 mOe by means of two concentric Moly-Permalloy shields manufactured by Allegheny Ludlum Steel Corp. The magnetometer was calibrated by externally applying a known magnetic flux to the primary L_p by means of a long thin solenoid placed in L_p and measuring the responding ΔI_f. The noise of the magnetometer is about 1.5×10^{-8} G cm^2 with a bandwidth of 10 kHz, while the dynamic range is 5×10^{-3} G cm^2.

The disk-shaped sample (about 1 cm diameter $\times 0.5$ mm thick) is thermally bonded to a 99.999% pure copper sample holder which in turn is thermally linked to a resistive heater and a Solitron germanium thermometer. The thermal link also acts as a mechanical link for rotating the sample about its axis through a bevel-gear arrangement (see Fig. 1). With this arrangement, a temperature resolution of 0.5 mK and a range of 1.8–4.2 K is achieved. The thermometer was calibrated versus helium vapor pressure. Using the bevel gear, a rotation of about 200° about the axis of the sample is possible without breaking the thermal links.

A superconducting niobium split solenoid, operating in persistent-current mode, surrounds the sample. It applies a magnetic field which can be made parallel to the plane faces of the sample disk by means of a control rod used to tip the magnet. A split solenoid is used to improve the spatial homogeneity of the field produced[20] and to facilitate mechanical linkage of the sample to the rotating gears. The magnet was calibrated using a thin rectangular tin plate of known dimensions and measuring the total flux expelled at the transition temperature in a given applied field. To reduce extraneous magnetic signals, drifts, and temperature-dependent magnetic effects, the parts of the apparatus close to the transporter or the magnet are constructed with 99.999% pure copper or with lead-free "red brass." Also, the thermometer and the heater with their twisted leads are placed outside the magnet, far away from the transporter primary. The remaining background (with zero applied field) temperature-dependent signal is measured and subtracted from the experi-

mental data before analysis. The sample temperature is swept up and down and only reversible data are used.

The samples used are single crystals of tin with known crystallographic orientations. They are slices cut from cylindrical crystals of the appropriate orientations. These cylindrical crystals are grown from 99.9999% pure tin (from Cominco American Inc.) by slowly recrystallizing the melted tin in contact with a seed crystal. Graphite molds are used; and a sliding furnace provides the thermal gradient and the means of "drawing" the crystal from the seed. Sample slices are cut from good sections of the crystalline cylinder using a Servomet (model SMD) spark cutter manufactured by the Metals Research Corp. After cutting, the sample disk is electropolished by a perchloric acid-acetic anhydride mixture to obtain flat polished faces. The smoothness of the surfaces is confirmed by the fact that they look dark under an optical microscope, indicating the absence of scattered light from any surface roughness. We do not expect tin to show the oxygen sensitivity and faceting effects leading to erroneous values of λ as discussed by Varmazis and Strongin[21] in connection with their work on Nb and Ta. Further confirmation of surface quality is provided by the consistent results found for λ in a number of samples polished in this way, while a larger value of λ was found for a sample intentionally measured without the full polishing treatment. Laue x-ray back-reflection pictures are taken off the surfaces to ascertain the crystal perfection of the sample as well as its orientation. Three orientations of crystals were grown, those with the sample normal $\hat{n} = \langle 001 \rangle$, $\langle 100 \rangle$, and $\langle 110 \rangle$. The residual resistance ratio of these crystals ranges from 2000 to 4000, implying that the ratio of the mean free path to the coherence length, l/ξ_0, ranges from 100 to 200. In this purity range, the penetration depth is not significantly dependent on l.

IV. EXPERIMENTAL RESULTS

The experimental procedure consists of (i) rotating the sample to the desired orientation; (ii) setting the magnetic field (about 1 Oe); (iii) changing the temperature of the sample while measuring the flux change detected by the magnetometer. To compare our results with previous work, it is conventional to plot the data versus $Y = (1 - t^4)^{-1/2}$. To do this a value for T_c has to be determined. Since at temperatures close to T_c, we expect λ to be linearly dependent on Y, we choose the value of T_c to satisfy this criterion. In practice, with a given estimate for T_c, the λ-Y curve is differentiated numerically and its slope calculated. The value of T_c which produces a horizontal line in the $d\lambda/dY$ plot at high Y ($Y > 3$) is chosen.

Owing to the complicated geometry of the disk-shaped sample and the rectangular sensing coil, it is difficult to compute the magnetic coupling between the sensing coil and the sample with high precision. We thus used the data obtained by Waldram[2] on tin for the final calibration of our magnetometer, after verifying that this calibration was consistent with our own best independent determination. Data from polycrystalline samples are used in this comparison to eliminate effects due to anisotropies. These data are plotted in Fig. 2. The error bars shown on the present data include errors due to uncertainties in T_c as well as experimental errors. Waldram's data extend only to $Y = 2$ due to difficulties with making zero-frequency corrections. He also assumed that the slope $d\lambda/dY$ would be constant at $Y = 2$. The present result shows that $d\lambda/dY$ has not reached its limiting value there. The data of Schawlow and Devlin[3] on a cylindrical single crystal are also presented for comparison.

Our single-crystal data can be classified according to the orientations of $\hat{n}$ and $\hat{j}$. For our samples, $\hat{n} = \langle 001 \rangle$, $\langle 100 \rangle$, or $\langle 110 \rangle$. For each $\hat{n}$, different directions of $\hat{j}$ perpendicular to $\hat{n}$ are used. Since only $d\lambda/dY$ can be measured absolutely in this experiment, the data will be presented in this form. They appear in Figs. 3–5. Note the increase of $d\lambda/dY$ near the zero-temperature limit ($Y = 1$). This is a consequence of the presence of the energy gap and was first observed by Schawlow and Devlin.[3] The experimental data for each $(\hat{n}, \hat{j})$ are checked for reproducibility as follows:

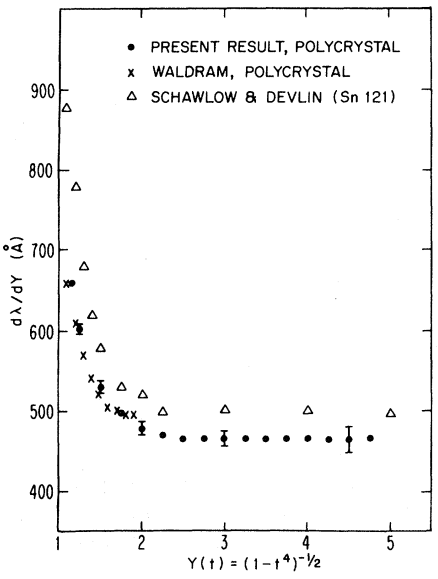

FIG. 2. Present polycrystalline data scaled to match Waldram's. Data of Schawlow and Devlin are also presented for comparison.

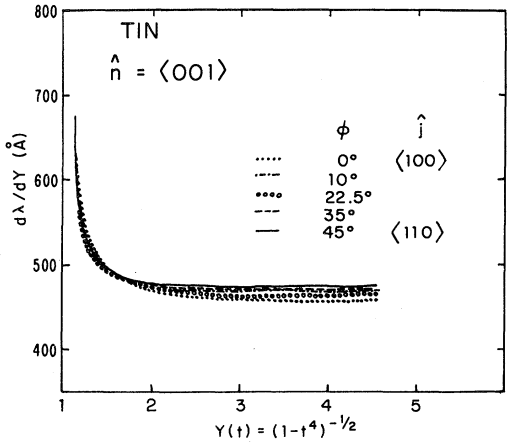

FIG. 3. $d\lambda/dY$ of tin with $\hat{n} = \langle 001 \rangle$. Five directions of $\hat{j}$ are plotted.

(i) Rotating the sample so that $\hat{j}$ is directed along a crystallographically equivalent orientation; sometimes this means a rotation of 180°;

(ii) Cutting another sample with the same $\hat{n}$ from the same crystal cylinder, or a separately grown crystal cylinder.

Figure 3 shows $d\lambda/dY$ for $\hat{n} = \langle 001 \rangle$ for five different orientations of $\hat{j}$. As seen in the figure any anisotropy present is not above errors in the data. This lack of anisotropy is reasonable because for this orientation the sample surface lies in a plane perpendicular to the tetragonal c axis and therefore has fourfold symmetry. The anisotropy due to $\hat{j}$ for a fixed $\hat{n}$ is a two-dimensional tensorial one and thus cannot exist in a plane with fourfold symmetry. Correspondingly the factor $\delta(\hat{n})$ in Eq. (11) is zero. The results for $\hat{n} = \langle 110 \rangle$ are presented in Fig. 4 for five direction of $\hat{j}$. The anisotropy is about 15%, significantly above estimated errors. The results for the third crystal with $\hat{n} = \langle 100 \rangle$ are plotted in Fig. 5. Unfortunately, this crystal has a broad superconducting transition, making the data of $d\lambda/dY$ near T_c unreliable. Thus only results in the low Y region ($Y \leq 3$, $t \leq 0.97$) are used. Only the extreme cases of $\hat{j} = \langle 001 \rangle$ and $\langle 100 \rangle$ are presented. Intermediate directions of $\hat{j}$ have data lying between these curves. The anisotropy is small.

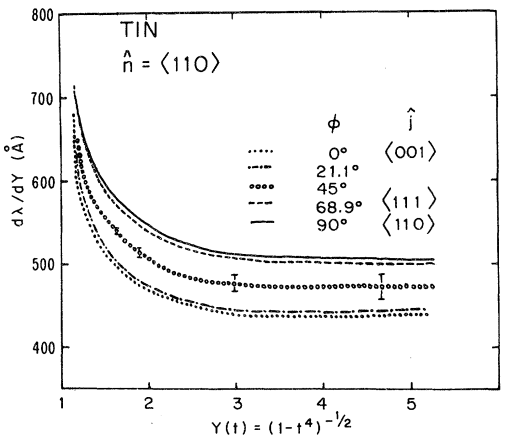

FIG. 4. $d\lambda/dY$ of tin with $\hat{n} = \langle 110 \rangle$. Five directions of $\hat{j}$ are plotted.

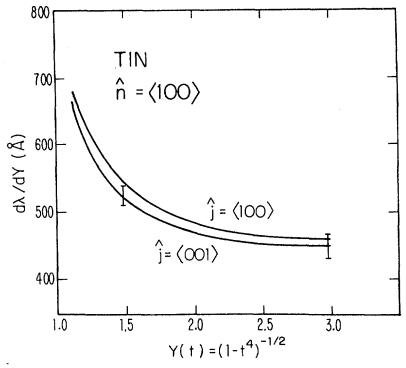

FIG. 5. $d\lambda/dY$ of tin with $\hat{n} = \langle 100 \rangle$. Two extreme directions of $\hat{j}$ are plotted.

The above results show directly the anisotropy of λ with respect to $\hat{j}$ for fixed $\hat{n}$. To illustrate the anisotropy with respect to $\hat{n}$, we compare data taken from crystals with different $\hat{n}$ but with $\hat{j}$ in the same direction. These are presented in Figs. 6–8. The case for $\hat{j} = \langle 110 \rangle$ with $\hat{n} = \langle 001 \rangle$ and $\langle 110 \rangle$ in Fig. 6 shows the largest anisotropy. The other two cases shown in Figs. 7 and 8 show anisotropies not much above estimated errors. However, in all cases, the anisotropy is biggest at low temperatures and gets smaller near T_c. This anisotropy with respect to $\hat{n}$ is the nonlocal anisotropy described in Sec. II. Near T_c, where the local limit is approached [see Eq. (7)], nonlocal anisotropy de-

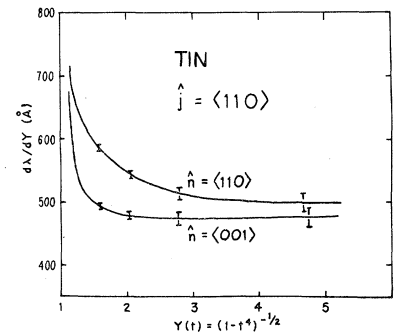

FIG. 6. $d\lambda/dY$ of tin with $\hat{j} = \langle 110 \rangle$ but with two different $\hat{n}$'s. Difference indicates nonlocal anisotropy.

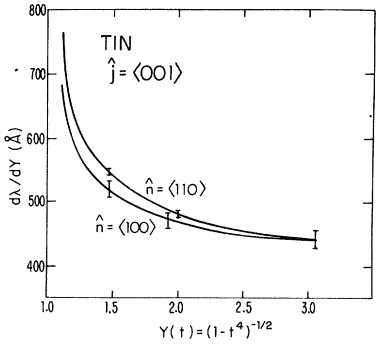

FIG. 7. $d\lambda/dY$ of tin with $\hat{j} = \langle 001\rangle$ but with two different $\hat{n}$'s. Difference indicates nonlocal anisotropy.

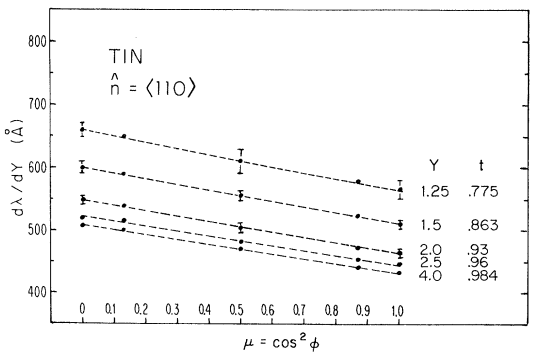

FIG. 9. $d\lambda/dY$ of tin with $\hat{n} = \langle 110\rangle$ plotted against $\cos^2\phi$, where ϕ is the angle between $\hat{j}$ and $\hat{c}$.

creases. One way to see this is that as $T \to T_c$, the ratio λ/ξ_0 is increased, and the angular width of the "effective" regions in the "ineffectiveness" picture increases, reducing the significance of the direction $\hat{n}$.

V. COMPARISON WITH THEORIES

Of the experimental data, those for $\hat{n} = \langle 110\rangle$ have the most anisotropy with respect to $\hat{j}$. They are thus chosen to be compared with the theory presented above. We plot $d\lambda/dY$ vs $\cos^2\phi$ for various temperatures in Fig. 9, where ϕ is the angle between $\hat{j}$ and $\hat{c}$. Linear plots are obtained, within experimental errors. This result follows from Eq. (12), and it supports the conclusion drawn there that for a fixed $\hat{n}$, the anisotropy of λ with respect to $\hat{j}$ is a two-dimensional tensorial one.

The quantitative theory of the nonlocal anisotropy of the penetration depth is a complicated one. As mentioned above in Sec. II, it is very difficult to incorporate the detailed anisotropies of the Fermi surface[11] and that of the energy gap[12] to calculate the penetration depth. We could find no anisotropic theoretical calculation which could be used to make a more quantitative comparison with our data. In view of this difficulty, we attempt to fit our data to the original BCS theory[9] by parameter fitting. Notwithstanding the limitations of such an approach, we still hope that our effort will produce some insight and incentive for further research.

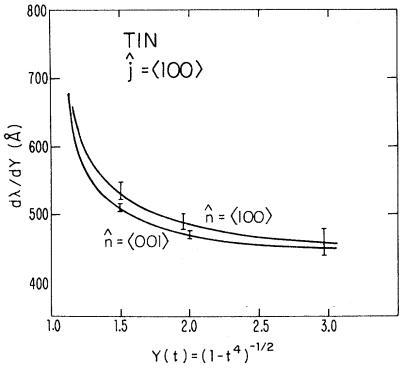

FIG. 8. $d\lambda/dY$ of tin with $\hat{j} = \langle 100\rangle$ but with two different $\hat{n}$'s. Difference indicates nonlocal anisotropy.

The following fitting procedure was adopted. First we calculate $\lambda_L(T)$ in the local limit by using Mühlschlegel's table.[22] To do this, we must assume values for $\lambda_L(0)$ and $\eta = 2\Delta(0)/kT_c$. $\lambda_L(0)$ will be one parameter we vary to fit the data. For η, we use one value for each direction $\hat{n}$. This reduced gap parameter η has been measured by experiments on acoustic attenuation and electron tunneling, among others. The measurements of Morse *et al.*[23] determined the average energy gap for electrons with velocities nearly perpendicular to the direction of the sound propagation. Their results of η are thus applicable to the present analysis in the nonlocal limit, where the "effective" electrons move nearly perpendicular to $\hat{n}$. They found the values of η averaged over electron velocities perpendicular to $\hat{n}$ to be $\eta = 3.1 \pm 0.1$, 3.5 ± 0.1, and 3.8 ± 0.1, for $\hat{n} = \langle 001\rangle$, $\langle 100\rangle$, and $\langle 110\rangle$, respectively. These values for η will be used here to compare with our data of the corresponding $\hat{n}$. The comparison will be limited to the low-temperature ($Y < 2.5$) region, where the nonlocal limit holds quite well. Using a value for η, the temperature dependence of the reduced London penetration depth $\lambda_L(T)/\lambda_L(0)$ is obtained by interpolating Mühlschlegel's table[22] assuming the BCS form for $\Delta(T)/\Delta(0)$. Then $\lambda_L(T)$ is calculated by scaling with $\lambda_L(0)$.

A value for the coherence length $\xi_0(\hat{n})$ is assumed for each direction $\hat{n}$. With this ξ_0, we compute the penetration depth λ by using the graphs of λ/λ_L versus ξ_0/λ_L plotted by Bardeen *et al.* (Fig. 7 in

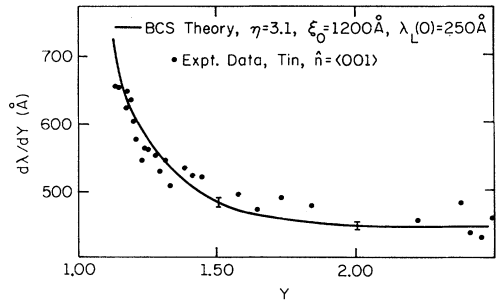

FIG. 10. Fit of the BCS theory with data for $\hat{n} = \langle 001 \rangle$.

Ref. 7). The graphs corresponding to the diffuse scattering limit are used since this limit seems to be a more realistic assumption experimentally. The original BCS plot has separate curves for the $T = 0$ and the $T = T_c$ limits. We use a curve which interpolates between these two curves in a way suitable for tin.[24] [It should be noted that this theoretical plot is based on asymptotic approximations of the kernel $K(q, T)$ in the limits of small and large q. More general approaches by Nam[14] and Halbritter[25] are free of this limitation, but they are more difficult to apply.] Using this interpolated curve of λ/λ_L vs ξ_0/λ_L, we calculate $\lambda(T)$ from the values of the parameters ξ_0 and $\lambda_L(T)$.

The slope $d\lambda/dY$ is then calculated by numerical differentiation. The results are fitted to the experimental data by varying the parameters ξ_0 and $\lambda_L(0)$. The slope $d\lambda/dY$ is used for fitting because it is more sensitive than $\lambda(Y)$ to changes in parameters and was measured absolutely in this experiment. The results of such fitting on the single crystal data can be seen in Figs. 10–12. The data for $\hat{n} = \langle 110 \rangle$ have significant anisotropy among the directions of $\hat{j}$ and these are thus presented separately in Fig. 12. The error bars refer to the errors in the theoretical calculation. The

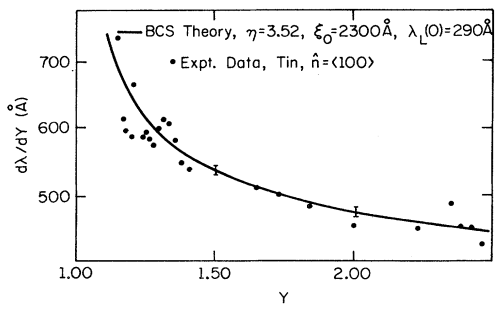

FIG. 11. Fit of the BCS theory with data for $\hat{n} = \langle 100 \rangle$.

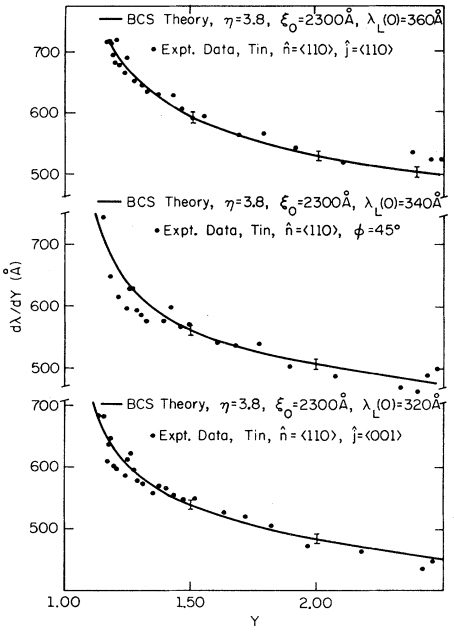

FIG. 12. Fit of the BCS theory with data for $\hat{n} = \langle 110 \rangle$ and three directions of $\hat{j}$. The plots have been shifted vertically for clarity. As in Fig. 9, ϕ is the angle between $\hat{j}$ and $\hat{c}$.

scatter in the experimental data points indicates the errors in the data. Both these errors are accentuated by the process of numerical differentiation. It should be emphasized that the reduced energy gaps $\eta = 2\Delta(0)/k T_c$ are obtained from ultrasonic attenuation data and are not adjusted to fit the data. The shape of $d\lambda/dY$ is quite sensitive to changes in η. Thus an uncertainty in the value of η would have a significant effect on the data fitting.

The directions $\hat{n} = \langle 100 \rangle$ and $\langle 110 \rangle$ require ξ_0 2300 Å, which is an accepted value.[5] The values for $\lambda_L(0)$ are close to the often quoted value of $\lambda_L(0)$ = 350 Å. The data for $\hat{n} = \langle 001 \rangle$ has a very sharp rise in $d\lambda/dY$ at low Y and this is why a low value for ξ_0 (= 1200 Å) has to be used to fit the data. Its low value for η(= 3.1) leads to a rapid increase in $\lambda_L(T)/\lambda_L(0)$ with temperature and thus a smaller $\lambda_L(0)$ is needed to compensate this effect. That $\hat{n} = \langle 001 \rangle$ is the tetragonal axis may be the cause of some of this unique behavior.

Finally, we should keep in mind again the possible danger of fitting anisotropic data to an isotropic theory by simply varying parameters, as well as the inadequacies of the simple BCS theory. However, the results obtained above are not unreasonable. It is hoped that this effort will stimulate interest and provide guidance to further research on the effects of crystalline anisotropies on the basic properties of superconductors.

*Supported in part by NSF, ONR, JSEP, and ARPA.
†Present address: Physics Department, University of Illinois, Urbana, Ill. 61801.
‡Present address: Department of Applied Physics, Stanford University, Stanford, Calif. 94305.

[1]A. B. Pippard, Proc. R. Soc. Lond. A 216, 547 (1953).
[2]J. R. Waldram, Adv. Phys. 13, 1 (1964), and references therein.
[3]A. L. Schawlow and G. E. Devlin, Phys. Rev. 113, 120 (1959).
[4]R. F. Gasparovic and W. L. McLean, Phys. Rev. B 2, 2519 (1970).
[5]For a review, see R. Meservey and B. B. Schwartz, in *Superconductivity*, edited by R. D. Parks (Dekker, New York, 1969), Chap. 3.
[6]P. C. L. Tai, M. R. Beasley, and M. Tinkham, in *Proceedings of the Thirteenth International Conference in Low Temperature Physics, Boulder, Colo.*, 1972, edited by W. J. O'Sullivan, K. D. Timmerhaus, and E. F. Hammel (Plenum, New York, 1974), Vol. 3, p. 740.
[7]F. London and H. London, Proc. R. Soc. Lond. A 149, 71 (1935).
[8]C. J. Gorter and H. B. G. Casimir, Z. Phys. 35, 963 (1934).
[9]J. Bardeen, L. N. Cooper, and J. R. Schrieffer, Phys. Rev. 108, 1175 (1957).
[10]A. B. Pippard, in *Advances in Electronics and Electron Physics*, edited by L. Marton (Academic, New York, 1954), Vol. VI, p. 1.
[11]G. Weisz, Phys. Rev. 144, 504 (1966); M. D. Staflew and A. R. de Vroomen, Phys. Status Solidi 23, 683 (1967).
[12]A. J. Bennett, Phys. Rev. 153, 482 (1967).
[13]V. A. Litovchenko, Fiz. Tverd. Tela 6, 1051 (1964) [Sov. Phys.-Solid State 6, 812 (1964)].
[14]Sang Boo Nam, Phys. Rev. 156, 470 (1967).
[15]P. C. L. Tai, Ph.D. thesis (Harvard University, 1973) (unpublished).
[16]A. B. Pippard, in *Low Temperature Physics*, edited by C. De Witt (Gordon and Breach, New York, 1962).
[17]A. B. Pippard, Proc. R. Soc. Lond. A 224, 273 (1954).
[18]R. Anderson and D. M. Ginsberg, Phys. Rev. B 5, 4421 (1972).
[19]J. P. Gollub, M. R. Beasley, R. Callarotti, and M. Tinkham, Phys. Rev. B 7, 3039 (1973).
[20]D. B. Montgomery and J. Terrel, *Some Useful Information for the Design of Air Core Solenoids* (National Magnet Laboratory Report, Cambridge, Mass., 1961).
[21]C. Varmazis and M. Strongin, Phys. Rev. B 10, 1885 (1974).
[22]B Mühlschlegel, Z. Phys. 155, 313 (1959).
[23]R. W. Morse, T. Olsen, and J. D. Gavenda, Phys. Rev. Lett. 3, 15 (1959); 3, 193 (E) (1959).
[24]The authors wish to thank Professor J. Bardeen for providing the tabulation of such an interpolated curve.
[25]J. Halbritter, Z. Phys. 243, 201 (1971).